

# Neural Lithography: Close the Design-to-Manufacturing Gap in Computational Optics with a 'Real2Sim' Learned Photolithography Simulator

CHENG ZHENG<sup>\*†</sup>, Massachusetts Institute of Technology, USA  
 GUANGYUAN ZHAO<sup>\*†</sup>, The Chinese University of Hong Kong, China  
 PETER T.C. SO, Massachusetts Institute of Technology, USA

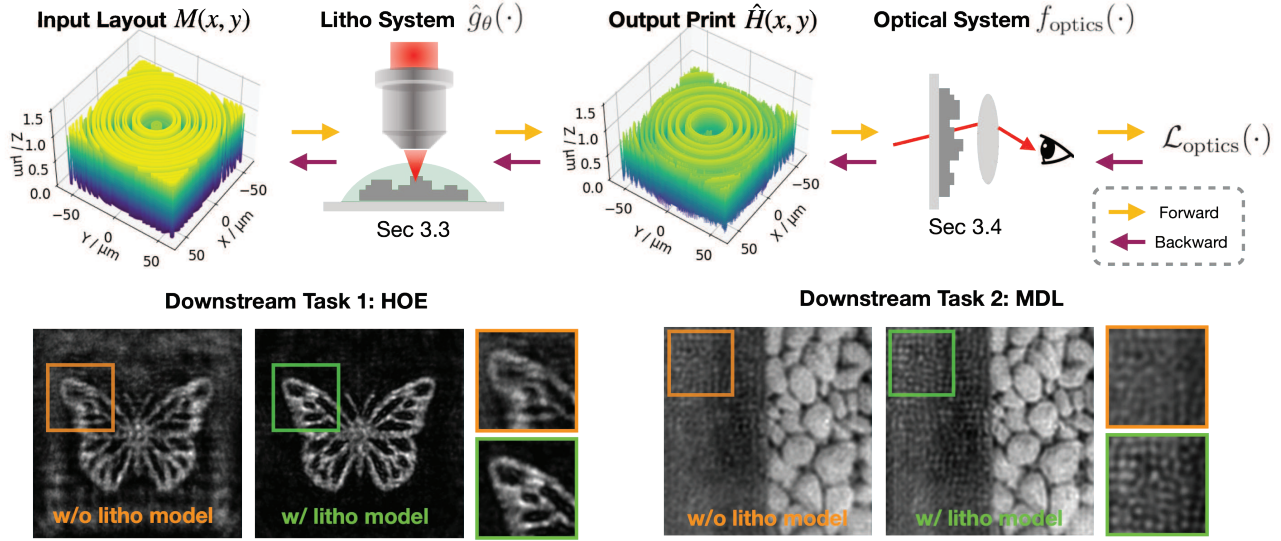


Fig. 1. **Our neural lithography framework for improving the image quality of fabricated optics.** We digitalize a real-world photolithography system via learning its digital twin  $\hat{g}_\theta$  (Sec. 3.3) from real measurements. This helps in revealing fabrication constraints during the downstream optical design tasks, including the task-specific light transport  $f_{\text{optics}}$  and metric  $\mathcal{L}_{\text{optics}}$  (Sec. 3.4). Our work showcases an improved performance on the design of holographic optical elements (HOE) and multilevel diffractive lenses (MDL) with our differentiable neural lithography simulator in the design loop.

We introduce neural lithography to address the ‘design-to-manufacturing’ gap in computational optics. Computational optics with large design degrees of freedom enable advanced functionalities and performance beyond traditional optics. However, the existing design approaches often overlook the numerical modeling of the manufacturing process, which can result in significant performance deviation between the design and the fabricated optics. To bridge this gap, we, for the first time, propose a fully differentiable design framework that integrates a pre-trained photolithography simulator into the model-based optical design loop. Leveraging a blend of physics-informed modeling and data-driven training using experimentally collected datasets, our photolithography simulator serves as a regularizer on fabrication feasibility during design, compensating for structure discrepancies introduced in the lithography process. We demonstrate the effectiveness of our approach through two typical tasks in computational optics, where we design and fabricate a holographic optical element (HOE) and a multi-level diffractive

lens (MDL) using a two-photon lithography system, showcasing improved optical performance on the task-specific metrics. The source code for this work is available on the project page: <https://neural-litho.github.io>.

CCS Concepts: • **Computer systems organization** → **Computational optics**.

Additional Key Words and Phrases: computational optics, computational lithography, computational imaging, end-to-end optimization, 3D printing

## 1 INTRODUCTION

In recent years, we have witnessed a revolution in the design of computational optical elements, extending well beyond conventional lenses and mirrors. Holographic optical elements, as a representative example, have found applications in various domains, including 3D imaging as speckle generators [Intel 2023], augmented reality as waveguide combiners [Jang et al. 2020, 2022], laser scanning as beam splitters [Hahn et al. 2020], and others [Kuo et al. 2020; Blachowicz et al. 2021]. Recent advances in deep learning and auto-differentiation [Baydin et al. 2018] have further enabled the development of end-to-end design pipelines for diffractive- [Sitzmann et al.

<sup>\*</sup>Corresponding author.  
<sup>†</sup>Equal contribution.

Authors’ addresses: Cheng Zheng, Massachusetts Institute of Technology, 77 Massachusetts Ave, Cambridge, MA, 02139, USA, chengzh@mit.edu; Guangyuan Zhao, The Chinese University of Hong Kong, Hong Kong, China, zhaoguangyuan2021@gmail.com; Peter T.C. So, Massachusetts Institute of Technology, 77 Massachusetts Ave, Cambridge, MA, USA, ptso@mit.edu.

2018] and meta-optical [Tseng et al. 2021] imaging systems, demonstrating promising results in numerous imaging tasks, such as depth from defocus [Ikoma et al. 2021], hyperspectral imaging [Baek et al. 2021], high-dynamic-range imaging [Metzler et al. 2020; Sun et al. 2020a], and image pixel super-resolution [Sitzmann et al. 2018; Sun et al. 2020b]. These computational imaging devices facilitate the creation of compact, miniaturized, and multifunctional imaging devices and expand the capabilities of conventional vision systems, offering unprecedented opportunities to meet diverse imaging requirements.

Nonetheless, a crucial challenge remains: fabricating elements that fulfill design objectives, offering large design degrees of freedom (DOF), and being cost-effective. Present popular fabrication techniques include e-beam lithography [Tseng et al. 2021], diamond tuning [Sitzmann et al. 2018], and photolithography [Levin et al. 2013; Tan et al. 2021; Boominathan et al. 2020; Orange-Kedem et al. 2021; Baek et al. 2021]. Among these techniques, photolithography, which is the focus of this work, uniquely allows 3D manufacturing capacity [Blachowicz et al. 2021; You et al. 2020], exhibits low cost, easy prototyping, and allows larger and flexible design space [Lee et al. 2023], which are more or less unmet in other fabrication methods. Yet, a critical step, the numerical modeling of the photolithography process in the design loop, is often overlooked in previous studies [Jang et al. 2020; Tan et al. 2021; Boominathan et al. 2020].

We identify this deficiency, a phenomenon we term the "**design-to-manufacturing gap**" in computational optics, as a fundamental issue in the current design and fabrication process. This gap, arising from differences between the theoretical and actual outputs of the lithography system due to light diffraction and photochemical processes, has significant implications [Wang et al. 2020; Roques-Carmes et al. 2022]. This impairs not only the accuracy of optical information processing, the diffraction efficiency [Ikoma et al. 2021; Baek et al. 2021] but also the minimum controllable feature size, which is a critical parameter in computational optics as it determines the maximum diffraction angle [Levin et al. 2013] and the étendue of the optical system [Kuo et al. 2020]. While an intuitive solution is to numerically incorporate the manufacturability during the task design process, developing a high-fidelity simulator to ensure flawless integration and efficiently co-optimizing the task-specific design process remains a further challenge.

In response to these challenges, we propose a framework that integrates a pre-trained neural lithography simulator into the model-based optical design process to collectively work with the task-related computational optics models to let the design meet task-specific metrics while maintaining fabrication feasibility. This simulator, trained from the dataset explored in a real-world lithography system using a synergistic blend of traditional physics-based and data-driven modeling, compensates for the deviation between the ideal and the real lithography process. In this way, our framework mitigates the "design-to-manufacturing gap" and enhances the fabrication fidelity of the design, leading to superior performance in downstream computational optical tasks.

Specifically, our contributions are:

- A "real2sim" methodology that learns high-fidelity neural simulators that accurately model real-world photolithography

systems from 2.5D atomic force microscope (AFM) measurements.

- A design and fabrication co-optimization pipeline that models the downstream computational optics task and photolithography process as two intersected differentiable simulators to optimize for desired optical performance post-manufacturing, using inline holography and imaging as example tasks.
- Experimental verification of improved optical performance by fabricating optimized diffractive optical elements with a two-photon lithography (TPL) system and evaluating on a home-built optical setup.

*Scope.* This research employs a 'Real2Sim' learning approach to construct high-fidelity neural photolithography simulators, specifically validated on TPL systems using AFM datasets. We take initial steps in the broad domain of co-optimizing manufacturability with computational optics design. We believe that the insights provided by our work are invaluable and could inspire further research in the fields of computational optics and photolithography.

## 2 RELATED WORK

**Model-based optical proximity correction (OPC) and inverse lithography technology (ILT)** are computational lithography techniques commonly used to compensate for errors due to diffraction or process effects during or after fabrication. Both methods are based on a simulator of the lithography system. The former refers to the solution of perturbing surrounding pixels of input design geometry through feedback from the simulator. The latter formulates the lithography enhancement task as an inverse design problem and sets the input design geometry as the targets with no limitation on the design DOF [Cecil et al. 2022]. Early research built a physics-based simulator of the lithography system and solved the ILT problem with adjoint methods/gradient descent/backpropagation [Cecil et al. 2022; Poonawala and Milanfar 2007]. Recently, researchers have been using deep learning methods, such as LithoGAN [Ye et al. 2019], GAN-OPC [Yang et al. 2018], and optics-inspired neural networks [Yang et al. 2022b,a], neural-ILT [Jiang et al. 2020] to speed up the OPC or ILT process through learning a fast proxy from expensive simulated data generated from the physics-based simulator.

Our work addresses a critical challenge in computational lithography: constructing a high-fidelity digital twin of real-world lithography systems. Such systems have been modeled in a white-box manner, building physics-based simulators approximated from first principles in optics and photochemistry, like the Hopkins diffraction model for Kohler illumination and sigmoid functions for resist photochemical reactions [Cobb et al. 1996; Poonawala and Milanfar 2007; Chevalier et al. 2021]. However, they fall short in adapting to system-specific and photoresist-specific variations [Arthur and Martin 1996]. These limitations are not fully remedied even for industry standards like Sentaurus Lithography, which has evolved to simulate 3D resist profiles [Synopsys 2023].

Against this backdrop, our research, while rooted in a learned representation of the lithography system, introduces a paradigm-shifting contribution that may significantly improve lithography

performance. We employ a 'real2sim' methodology<sup>1</sup> for training our differentiable simulator from real 2.5D layout-print pairs, in contrast with the conventional 'sim2sim' method. Therefore, our method offers a more adaptable and accurate way to digitalize the photolithography system while de-emphasizing the computational speed. Furthermore, our focus on 3D structures necessitates a more informative dataset – a '2.5D' heightmap of prints instead of '2D' datasets for common edge position error (EPE) corrections [Cecil et al. 2022].

**Optimization of photolithography for micro/nano optics** has seen recent advancements (Table 1). Wang et al. utilized grid search for Dammann gratings fabrication [Wang et al. 2020], while Lang et al. implemented a parameterized physics model for multi-photon lithography [Lang et al. 2022]. Chevalier et al. integrated a physics-based lithography model to optimize microlens array fabrication using atomic force microscopy data [Chevalier et al. 2021; Giessibl 2003]. Of particular relevance is Liao et al.'s work [Liao et al. 2022], which leveraged machine learning to construct an i-line lithography simulator from real 2D binary scanning electron microscopy (SEM) data, leading to a non-differentiable OPC to optimize for the EPE. However, this process presents computational challenges, and the limited SEM dataset information hinders complex design capabilities.

	[Wang et al. 2020]	[Chevalier et al. 2021]	[Lang et al. 2022]	[Liao et al. 2022]	Ours
Data-driven	✓	✗	✓	✓	✓
Physics	✓	✓	✓	✓	✓
2.5D	✓	✓	✓	✗	✓
Nanoscale	✓	✓	✗	✓	✓
End-to-end∇	✗	✗	✗	✗	✓

Table 1. Comparison of photolithography optimization approaches on fabricating the micro-/nano-optics along the axes of data-driven modeling, physics-aware modeling, 2.5D optimization capability, nanoscale precision, and end-to-end differentiability.

In contrast, our work employs a dataset measured by AFM, enabling optimization for 2.5D geometry of computational optics. Furthermore, our approach is fully differentiable, combining optical design and fabrication correction end-to-end. By incorporating fabrication constraints directly in the design loop, this methodology navigates complex design space more effectively.

**Differentiable optics** refers to an emerging technique in computational optics that models an optical system with chained differentiable functions to design optical systems using gradient-based optimization methods, which is computationally efficient and effective in exploring large and complex design space. Recently, based on differentiable optics, a large body of work in computational imaging has studied the joint design of the optics and the reconstruction algorithms [Sitzmann et al. 2018; Tseng et al. 2021] using the physics-based (white-box) simulators.

Our neural/differentiable lithography also lies in the regime of differentiable optics. The uniqueness is that our work is the first to integrate design and manufacturing as two differentiable modules of

<sup>1</sup>real2sim is an emerging concept in robotics which advocates for building high-fidelity simulators directly from real-world data [ICRA 2023].

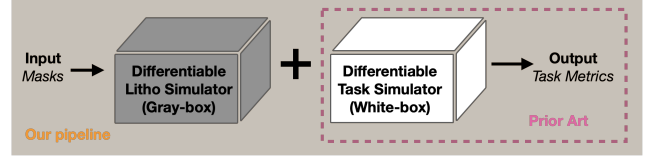


Fig. 2. Our work advances the differentiable optics via chaining the prior art of white-box design with a gray-box lithography simulator. The task simulator uses the first principles of optics to build the task light transport. We add a 'real2sim' learned gray-box lithography simulator in the design loop.

an end-to-end optimization pipeline for high-performance computational optics tasks (Fig. 2). We, on the one hand, utilize the differentiable optics-based first principle to enable the optical design and, on the other hand, build a differentiable neural lithography simulator in a 'real2sim' manner (the gray-box simulator) for the lithography process. The latter resembles very recent work on 'hardware-in-the-loop' optimization of camera ISP [Tseng et al. 2019] and holographic display system [Peng et al. 2020; Chakravarthula et al. 2020].

### 3 METHODOLOGY

We formulate the problem of the fabrication-embedded design of computational optics in subsection 3.1. We then detail our solution of using model-based optimization for jointly optimizing the fabrication and the design process in subsection 3.2. We illustrate our protocol for digitalizing the lithography system in subsection 3.3. Next, we present two tasks of designing and fabricating holographic optical element (HOE) and multi-level diffractive lens (MDL) in subsection 3.4.

#### 3.1 Problem statement

We are interested in finding a mask layout  $M(x, y)$  to feed into a photolithography system, such that the output fabricated structure being used as an optical element with height profile  $H(x, y) = g(M(x, y))$  achieves the best performance in the downstream computational optics tasks, where  $g$  denotes the underlying mathematical representation of the fabrication process. The whole pipeline is described as follows:

$$M^*(x, y) = \arg \min_{M(x, y)} \mathcal{L}_{\text{optics}}(f_{\text{optics}}(g(M(x, y)))). \quad (1)$$

Without loss of generality, we use  $f_{\text{optics}}$  and  $\mathcal{L}_{\text{optics}}$  to represent the task-specific forward light transport and loss function of the downstream tasks, respectively.

The manufacturing process, denoted by  $g$ , is pivotal for the overall pipeline's efficacy. While past research in computational optics often views this process as an identical mapping,  $g(M(x, y)) = M(x, y)$  [Tan et al. 2021; Boominathan et al. 2020; Jiang et al. 2020], this assumption falls short for features around the diffraction limit. In the photolithography process, the light's diffraction, system aberrations, and chemical reactions cause deviations from the input layout, negatively impacting the performance of the fabricated computational optics, which depends significantly on precise structure

geometry. We focus on creating computational optics with desired optical performance post-manufacturing.

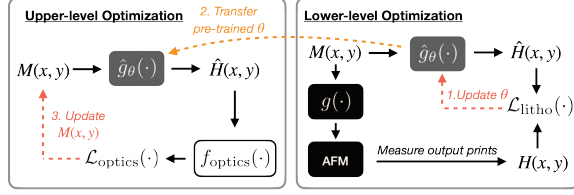


Fig. 3. **Bilevel optimization in neural lithography.** The upper-level optimization optimizes the mask  $M(x, y)$  while the lower-level optimization optimizes the litho digital twin  $\hat{g}_\theta$ , the result of which is imported and fixed as a constraint in the upper-level optimization.

### 3.2 Model-based differentiable optimization of computational optics with a lithography simulator

Our solution reformulates the objective in Eq. 1 as a bi-level optimization problem in Fig. 3 [Colson et al. 2007], structured as:

**Upper-level (Leader) optimization (subsec. 3.4):** *Optimize the performance of the computational optics in the specific task based on predictions from the learned lithography simulator (e.g., minimize wavefront error, maximize optical efficiency, or achieve desired functionality).* The objective function in Eq. 1 is rewritten as:

$$M^*(x, y) = \arg \min_{M(x, y)} \mathcal{L}_{\text{optics}}(f_{\text{optics}}(\hat{g}_\theta(M(x, y)))), \quad (2)$$

where we substitute the unknown underlying lithography system  $g$  in Eq. 1 with  $\hat{g}_\theta$ , a digital twin of  $g$  with parameters  $\theta$  learned in the lower-level optimization.

**Lower-level (Follower) optimization (subsec. 3.3):** *Pre-train a lithography digital twin  $\hat{g}_\theta$  that accurately predicts height profile  $H(x, y)$  of the printed structure given input layout  $M(x, y)$ .* The optimization process is minimizing the difference between the lithography simulator prediction  $\hat{H}(x, y) = \hat{g}_\theta(M(x, y))$ , and the experimentally measured 2.5D continuous height  $H(x, y)$ :

$$\theta^* = \arg \min_{\theta} \mathcal{L}_{\text{litho}}(H(x, y), \hat{H}(x, y)), \quad (3)$$

where  $\mathcal{L}_{\text{litho}}$  denotes the loss function for this supervised learning, and here we use the mean absolute error.

**To summarize:** The leader problem optimizes computational optical element design using the prediction from the neural lithography simulator, learned independently in the follower problem. These interconnected problems, addressed in a bilevel optimization framework, close the design-to-manufacturing gap with robust designs and better optical performance.

### 3.3 'Real2Sim' learning a neural lithography simulator

**3.3.1 Lithography forward model.** We construct a physics-based neural network  $\hat{g}_\theta$  as the differentiable digital twin of the lithography system  $g$ , referred to as the physics-based learning (PBL) model in this paper. The modeling of the photolithography process normally consists of an optical model and a resist model [Cobb et al. 1996; Chevalier et al. 2021; Lang et al. 2022]:

- The **optical model** calculates the light exposure dosage distribution on the photoresist, leading to the aerial image;
- The **resist model** models the photo-chemical reaction and development processes, leading to the final resist profile.

We first illustrate  $\hat{g}_\theta$  in the context of the general photolithography model and then detail the specific arrangements of the TPL system used in this work. In our context, **the resist profile is the ultimate fabricated structure**, as it does not undergo further processing steps. Inspired by the work from [Tseng et al. 2022] on photo-finishing, we also apply the pointwise and areawise neural networks inside  $\hat{g}_\theta$  to model the corresponding operations, respectively (see details in Supplements). Anatomy of the model  $\hat{g}_\theta$  is visualized in Fig. 4 and details of the sub-models are:

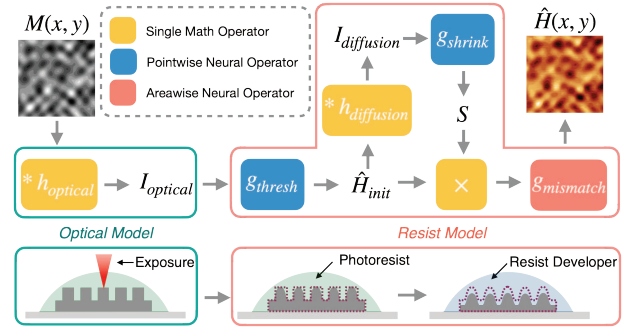


Fig. 4. **Anatomy of our litho digital twin  $\hat{g}_\theta : M(x, y) \rightarrow \hat{H}(x, y)$ .** The input layout  $M(x, y)$  goes through the optical model (exposure process) and resist model (photochemical reaction and development processes). The litho digital twin predicts the final fabricated structure height as  $\hat{H}(x, y)$ .

The **optical model**  $g_{\text{illum}}$  transforms the input layout mask  $M(x, y)$  into an exposure dosage distribution, also known as aerial image,  $I_{\text{aerial}}(x, y) = g_{\text{illum}}(M(x, y))$ . Depending on the illumination sources,  $g_{\text{illum}}$  normally incorporate illumination kernel(s), such as a Gaussian point spread function (PSF) under point-source illumination [Auzinger et al. 2018; Saha et al. 2017] or a series of convolution kernels decomposed from transmission-cross coefficient (TCC) matrix in Hopkin’s formulation under Köhler’s illumination [Cobb et al. 1996; Liao et al. 2022]. Specifically, in the point-scanning TPL system used in this work [Harinarayana and Shin 2021],  $g_{\text{illum}}$  is modeled as convolution between the mask  $M$  and a Gaussian PSF  $h_{\text{optical}}$  with a hyper-parameter  $\sigma_{\text{optical}}$  being its half-width at half maximum.

The **resist model** computes the photochemical reaction during exposure and accounts for the structure deformation during development. *The initialization of photochemical reaction process* is modeled with a pointwise neural network  $g_{\text{thresh}}$  to accurately handle the pixel-wise thresholding operation, resulting in the initial resist profile  $\hat{H}_{\text{init}}(x, y) = g_{\text{thresh}}(I_{\text{aerial}}(x, y))$ . Since the *diffusion of reactants* introduces cross-talk between nearby printed features, we use a Gaussian kernel  $h_{\text{diffusion}}$  with a learnable standard deviation  $\sigma_{\text{diffusion}}$  to approximate the spatial extent of diffusion [Lang et al. 2022]. As a result, at the end of the reaction we have:

$$I_{\text{diffusion}}(x, y) = \left( \hat{H}_{\text{init}} * h_{\text{diffusion}} \right) (x, y). \quad (4)$$



The *development process* introduces extra deformation to the printed structure, which has been observed to be unidirectional shrinkage perpendicular to the substrate due to the dissolution of soluble components and the capillary forces during the drying process [Meisel et al. 2006; D'Silva et al. 2021]. We model this anisotropic shrinkage  $S$  with an operation  $g_{\text{shrink}}$  represented by another point-wise neural network, giving  $S(x, y) = g_{\text{shrink}}(I_{\text{diffusion}}(x, y))$ . Thus, the resist profile is the product of  $\hat{H}_{\text{init}}$  and  $S$  after development.

To further mitigate mismatch from the above approximations, we introduce an areawise neural network as a learnable operator  $g_{\text{mismatch}}$ , giving the final fabricated structure as:

$$\hat{H}(x, y) = g_{\text{mismatch}}((\hat{H}_{\text{init}} \cdot S)(x, y)). \quad (5)$$

**Chaining the sub-models**, we get the predicted height profile of the fabricated structure as:

$$\hat{H}(x, y) = \hat{g}_{\theta}(M(x, y)), \quad (6a)$$

$$= g_{\text{mismatch}}\left(\hat{H}_{\text{init}} \cdot g_{\text{shrink}}(\hat{H}_{\text{init}} * h_{\text{diffusion}})\right), \quad (6b)$$

$$\hat{H}_{\text{init}}(x, y) = g_{\text{thresh}}(g_{\text{illum}}(M(x, y))). \quad (6c)$$

When applying the 'real2sim' pipeline to diverse photolithography processes, one cannot rely on a 'one-size-fits-all' model. To effectively accommodate system-specific or process-dependent variations, hyper-parameters or operations must be fine-tuned. Key among these are  $h_{\text{optical}}$  or  $g_{\text{illum}}$  (pertaining to the illumination system) and  $h_{\text{diffusion}}$  (associated with the photoresist and its processing protocol). More details about the model architecture and the training process are in the Supplements.

**3.3.2 Constructing dataset for learning a lithography simulator.** To learn parameterized  $\hat{g}_{\theta}$  that enables the optimization of structure, we collect the first 2.5D dataset  $\mathcal{D} = \{(\mathbf{M}_i, \mathbf{H}_i)\}_{i=1}^N$  in photolithography, where  $N = 96$  is the size of the dataset,  $\mathbf{M}_i \in \mathbb{Z}_{\leq 12}^{n_1 \times n_2}$  is a random input layout and  $\mathbf{H}_i \in \mathbb{R}^{n_1 \times n_2}$  is the height profile of the fabricated structure, fabricated by a TPL system (Photonic Professional GT2, Nanoscribe GmbH), and measured offline by AFM. Here  $n_1 \times n_2 = 256 \times 256$  is the lateral size of the structure. Since the slicing distance along the height direction is  $0.1 \mu\text{m}$ , and we have 12 levels in our fabrication, the input layouts represent discrete height values from 0 to  $1.2 \mu\text{m}$ , providing a phase modulation range from 0 to  $2.07\pi$  given a refractive index difference  $\Delta n = 0.548$  between the fabricated structure and air and illumination wavelength  $\lambda = 0.6328 \mu\text{m}$ . We register every AFM image  $\mathbf{H}_i$  with its corresponding input layout  $\mathbf{M}_i$  with the aid of homography estimation. Fig. 5 shows an example data pair. Details on the fabrication and characterization of the prints are in the Supplements.

### 3.4 End-to-end co-optimizing design and manufacturability in computational optics

We validate the performance of neural lithography with two representative tasks in computational optics. Below, we present the light transport and design pipeline for each task in Fig. 6. Due to the low absorption property of the fabricated optical element [Li et al. 2019], we treat it as a thin phase object with phase profile

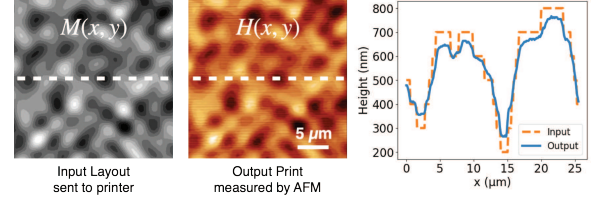


Fig. 5. An example of the experimental dataset for learning a neural lithography simulator. The line profiles along the white dashed lines show a clear height deviation between the input layout and the output print.

$\phi(x, y) = \frac{2\pi\Delta n}{\lambda} H(x, y)$ . Our work focuses on accurate  $H(x, y)$  and omits the variation in  $\Delta n$  as it was reported to be below 0.003, the phase variation induced by which is much smaller than that caused by variation of  $H(x, y)$  [Dottermusch et al. 2019]. In the design, we use the output  $\hat{H}(x, y)$  from our lithography digital twin  $\hat{g}_{\theta}$  for  $H(x, y)$  and optimize  $M(x, y)$  via auto-differentiation through wave-optics-based forward light transport. We utilize the Gumbel-Softmax reparameterization trick [Jang et al. 2016] to differentiate through the discrete design layout  $M \in \mathbb{Z}_{\leq 12}^{n_1 \times n_2}$  (see details in Supplements).

**3.4.1 Holographic optical element.** A holographic optical element (HOE) is a micro-structured optical component that generates a desired image or diffraction orders and is commonly used in beam splitting, 3D imaging/display, and augmented reality. We design a HOE for an inline holography system, where the fabricated HOE is expected to generate a pre-designed holographic image at imaging distance  $\Delta z = 300 \mu\text{m}$  upon plane wave illumination. We substitute  $f_{\text{optics}}$  in Eq. 1 with  $f_{\text{holo}}$  that calculates the intensity of the electric field  $I_{\text{out}}$  after free-space wave propagation of distance  $\Delta z$  with Rayleigh-Sommerfeld convolution [Goodman 2005]:

$$I_{\text{out}}(x, y) = f_{\text{holo}}(\phi(x, y)), \quad (7a)$$

$$= \left| e^{j\phi(x, y)} * h_{\Delta z}(x, y) \right|^2, \quad (7b)$$

where  $h_{\Delta z}(x, y) = \frac{\Delta z}{2\pi r^2} \left( \frac{1}{r} - \frac{j2\pi}{\lambda} \right) e^{\frac{j2\pi r}{\lambda}}$  is the propagation kernel with  $r = \sqrt{x^2 + y^2 + \Delta z^2}$ . Given a target holographic image  $I_{\text{target}}$ , the loss function  $\mathcal{L}_{\text{holo}}$  is:

$$\mathcal{L}_{\text{holo}}(I_{\text{target}}, I_{\text{out}}) = \mathcal{L}_{\text{rmse}}(I_{\text{target}}, I_{\text{out}}) + 0.1(1 - \eta_{\text{eff}}(I_{\text{out}})), \quad (8)$$

where  $\mathcal{L}_{\text{rmse}}$  is the root mean square error loss,  $\eta_{\text{eff}}(I_{\text{out}})$  is the energy efficiency, calculated as the sum of intensity inside the region of  $I_{\text{target}} > 0$  at image plane divided by the sum of total illumination light intensity.

**3.4.2 Multi-level diffractive lens.** Compared to conventional refractive lenses, diffractive lenses can perform imaging tasks while being lightweight and compact [Banerji et al. 2019]. We design MDLs with focal length  $\Delta z_f = 400 \mu\text{m}$  and object to lens distance is  $\Delta z_{\text{ol}} = 140 \text{mm}$ . The system's point spread function (PSF)  $I_{\text{psf}}$  is the intensity field illuminated by a point source at the object plane. In the context of incoherent imaging under paraxial approximation, the image formation is a shift-invariant convolution of the object  $I_{\text{obj}}$  with  $I_{\text{psf}}$ , and the camera records:

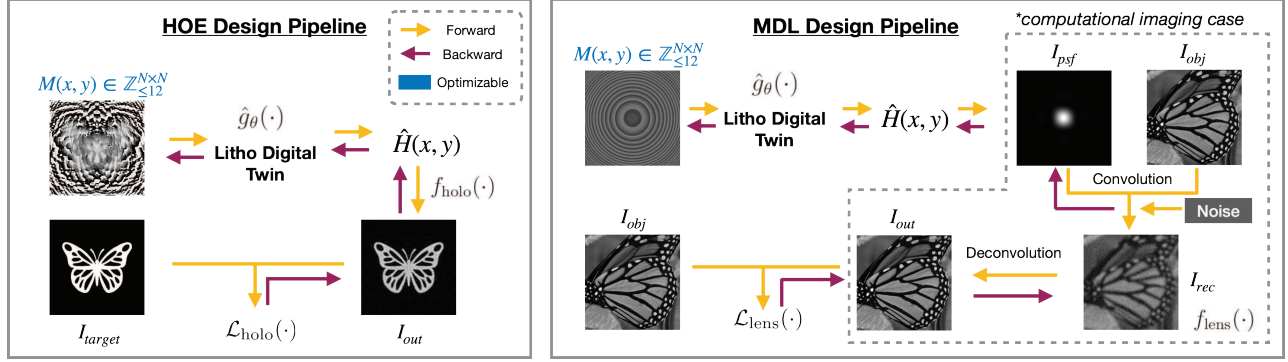


Fig. 6. Design pipelines of holographic optical elements (HOE) and multi-level diffractive lens (MDL).

$$I_{rec}(x, y) = \left| e^{j\phi(x, y)} * h_{\Delta z_f}(x, y) \right|^2 * I_{obj}(x, y) + \eta, \quad (9a)$$

$$= I_{psf}(x, y) * I_{obj}(x, y) + \eta, \quad (9b)$$

where  $\eta \sim \mathcal{N}(0, \sigma^2)$  is additive Gaussian readout noise. The propagation from the object to the lens is ignored in the  $I_{psf}$  calculation because  $\Delta z_{ol}$  is much larger than the diameter of the lens ( $120\mu\text{m}$  in our case) and we can assume the wavefront from the point source to be flat. Here, we design two types of MDL. The first one is for direct imaging without post-processing the acquired camera recording  $I_{rec}$ , and design metric  $\mathcal{L}_{lens}$  is the focusing efficiency [Banerji et al. 2019] of  $I_{psf}$ ; the second one is for in-direct imaging (namely, computational imaging), where we assess the imaging quality after deconvolving  $I_{rec}$  by  $I_{psf}$ .

**Direct imaging:** We calculate the PSF's center-to-background signal ratio (CBR)  $r_{cbr}$  and the corresponding loss function  $\mathcal{L}_{lens}(I_{psf}) = -\log(r_{cbr})$ . Considering that we have a numerical aperture  $NA \approx 0.15$ , corresponding to a diffraction-limited focal spot size of  $\approx 4\mu\text{m}$ , we choose center region size to be  $1\mu\text{m} \times 1\mu\text{m}$  and we empirically find this setting leads to the sharpest PSF after the optimization.

**In-direct/computational imaging:** We evaluate the image quality after post-processing [Sitzmann et al. 2018; Tseng et al. 2021]. we apply a fixed Richard-Lucy deconvolution process and calculate the mean absolute error (MAE) between the ground truth  $I_{obj}$  and deconvolved result as the loss  $\mathcal{L}_{lens}$ :

$$\mathcal{L}_{lens}(I_{rec}, I_{obj}) = \mathcal{L}_{mae}(f_{deconv}(I_{rec}, I_{psf}), I_{obj}), \quad (10)$$

where  $f_{deconv}$  denotes the deconvolution process, and in this work, we use the Richard-Lucy deconvolution algorithm [Zhao et al. 2018] with 50 iterations.

## 4 RESULTS

We first evaluate the accuracy and generalizability of our neural lithography simulator in subsection 4.1 (lower-level optimization). Then we present the results of designed and fabricated optical elements in computational optics tasks, in subsections 4.2 and 4.3 (upper-level optimization), which show the priority of our pipeline in mitigating the design-to-manufacturing gap. We further provide detailed results to visualize the improvement by our pipeline in

subsection 4.4 and noise analysis to investigate the performance limit of our method in subsection 4.5.

### 4.1 Forward predicting capability

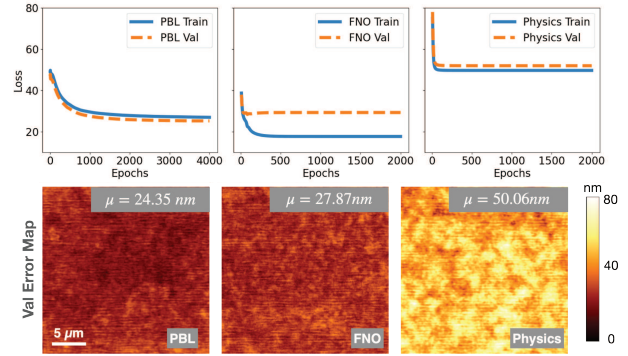


Fig. 7. Forward predicting capability of the  $\hat{g}_\theta$ . Top: The training and validation loss curves correspond to the three models explored in our work. Bottom: The corresponding average validation error map and the mean error value across the map.

We evaluate the efficacy for  $\hat{g}_\theta$ , trained from the dataset described in section 3.3.2 and Fig 5. We visualize the loss curves and error maps that compare our PBL model with other learnable modeling approaches, including the parameterized physics model [Lang et al. 2022] and Fourier Neural Operator (FNO) [Yang et al. 2022b]. The details of the models and training hyperparameters are in the Supplements. We show that the PBL modeling receives the lowest validation loss and error. The parameterized physics model has limited degrees of freedom and thus cannot fully fit the data. Without applying the physics model as a prior, FNO exhibits good fitting ability while tending to overfit on the training set.

### 4.2 Application: Holographic optical element

We design several HOEs with the three lithography models using the pipeline in subsection 3.4.1. The traditional design without a lithography model in the loop is also added as a reference. The designed input layouts are  $102.4\mu\text{m} \times 102.4\mu\text{m}$  with an optimizable

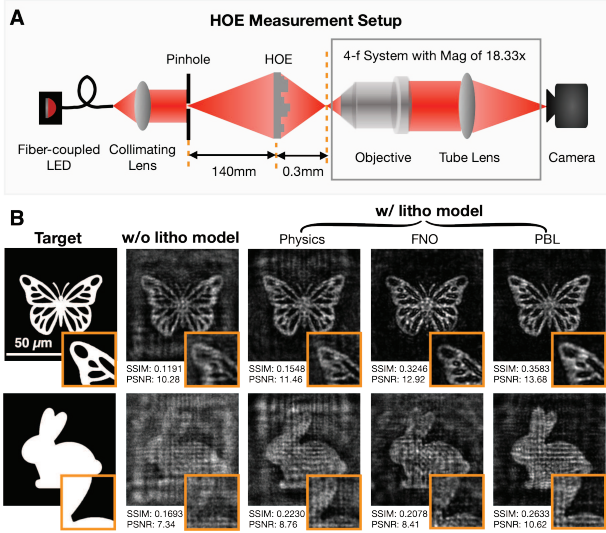


Fig. 8. **Performance of the designed HOE.** A: Sketch of the setup for characterizing the performance of HOE. B: Performance comparison shows that with the lithography model, the quality of the holographic images is improved, and the PBL model brings the most pronounced improvement.

pitch size of  $0.4\mu\text{m}$  and optimized with Adam for 1000 iterations under a learning rate of 0.1. We capture holographic images of the fabricated HOEs with the setup sketched in Fig. 8A. As expected, the resulting images with lithography models present better image quality and contrast. We also assess the SSIM and PSNR of the images using the Kornia package [Riba et al. 2020], where the one optimized using the PBL model scores the highest. The overall low value of the SSIM and PSNR may come from the measurement system’s misalignment and the layout’s limited quantization levels.

### 4.3 Application: Multi-level diffractive lens

We compare the performance of our designed and fabricated MDLs to investigate the performance gain brought by the neural lithography (Fig. 9). The designed MDL layouts are  $120\mu\text{m} \times 120\mu\text{m}$  with an optimizable pitch size of  $0.1\mu\text{m}$  and optimized with AdamW for 1000 iterations under a learning rate of 3. We built a system sketched in Fig. 9A, where the pinhole is used to calibrate the PSF of the imaging system. During imaging, we switch the light path to the object plane (the OLED display), which is in conjugation with the pinhole plane.

The **direct imaging** outcomes (Fig. 9B) demonstrate the imaging contrast bolstered by the PBL lithography simulator’s inclusion in the design loop. Further profiling of PSFs associated with various MDLs reveals that the design aided with the PBL model yields the brightest PSF. Furthermore, the **computational imaging** result in Fig. 9C shows that when both deconvolving with the camera-captured (calibrated) PSFs, the one with the neural lithography simulator results in more details, which retains the higher-frequency imaging capability, as highlighted in the zoom-in view. Post-calibration has been used to mitigate fabrication inaccuracy in previous work [Tseng et al. 2021], but the comparison here shows that it cannot fully address the issue. This is also evidenced by the

Fourier spectrum of the PSFs shown on the right-hand side of Fig. 9C, where the Fourier spectrum corresponding to the PSF associated with the PBL litho model exhibits higher frequency coverage.

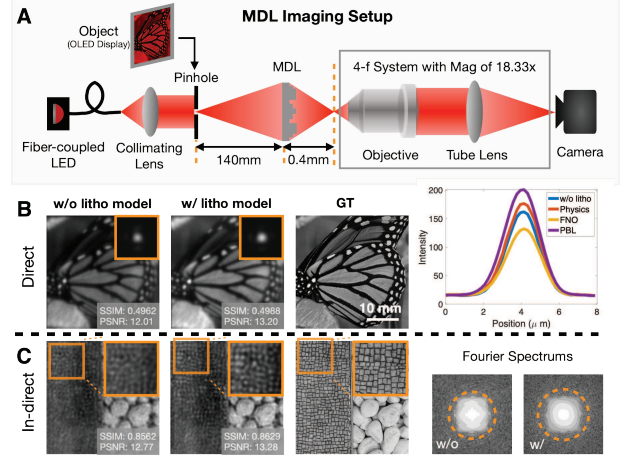


Fig. 9. **Imaging performance with the designed MDL.** A: Sketch of the setup for characterizing the performance of MDL. B: We show our measured PSFs and direct imaging results (i.e., w/o deconvolution) corresponding to design w/o and w/ PBL litho model. The end of this row shows the line profiles of PSFs designed w/o or w/ different litho models. C: Computational/Indirect Imaging result of the MDL. The lower right compares the Fourier spectrum of the designed PSFs. Our method’s design enhances the contrast in direct imaging (B) and the high-frequency imaging performance in computational imaging (C).

### 4.4 Design-to-manufacturing gap mitigation

In Fig. 10, we show the layout of the designed HOEs and optical micrographs of the corresponding fabricated structure. We observe more high-frequency features in the designs without the lithography model and a smoother profile in the designs with the lithography model. Also, there is a better coincidence between designs and prints when using our PBL lithography model in the design loop. In contrast, a large mismatch exists between design and print without a neural photolithography simulator. This evidences the lithography model serves as a regularizer on fabrication feasibility during the design process.

A quantitative comparison of the holographic images of the HOEs (micrographs of which are in Fig. 10) in both design and experiment in Fig. 11 reinforces our conclusion. The ones without the lithography model show the highest SSIM in the design while being the worst in the experimental measurement. Given the huge design-to-manufacturing gap in Fig. 11, it is unsurprising. The images using our neural photolithography simulator show the highest SSIM in manufacturing while maintaining the lowest gap between the design and manufacturing values. The comparison between the *Physics* and *PBL* models in the figure reveals that the *PBL* model does more than just add parameterized smoothness to the design profile, as the *Physics* model does. Instead, it captures more complex physical relationships, thereby better mitigating the design-to-manufacturing gap.



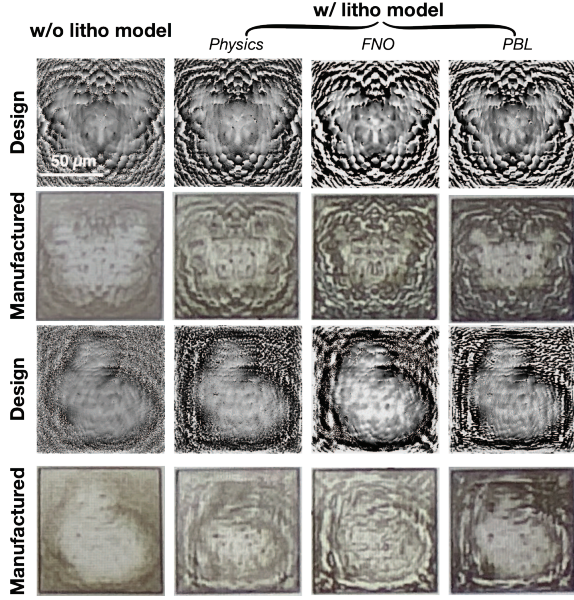


Fig. 10. **Qualitative comparison on the images of designed HOE and the corresponding fabricated structures.** The designed structure from one w/ litho model shares more similarity with their fabricated correspondences. Designs w/o the litho model render too fine-detail layout mask, the fabricates of which deviate a lot from the original designs. The slight difference in optical micrograph color tones comes from non-uniform illumination.

Similarly, the effectiveness of our method in creating multi-level diffractive lenses is evidenced by the PSFs displayed in Fig. 12. In both direct and computational imaging scenarios, the line profiles across the center of the PSFs from MDLs designed using the lithography model show a better fit to the design than those lacking the lithography model. Additionally, in the direct imaging case, the PSF with the lithography model displays higher overall brightness. In the computational imaging case, there is greater correspondence between the design and the resulting optical micrograph when using the lithography model.

#### 4.5 Analyze noise to the aleatoric uncertainty

The ultimate predicting ability of our lithography simulator depends on both the model’s learning ability and the dataset’s quality, relating to the model’s epistemic uncertainty and the dataset’s aleatoric uncertainty, respectively [Hüllermeier and Waegeman 2021]. In Fig. 13, we visualize and quantify noises by fabricating a flat surface (Fig. 13B) and a 5-step structure (Fig. 13C) and measuring them together with a flat substrate (Fig. 13A). *Comparison between Fig. 13A and Fig. 13B shows that the unmodeled fabrication error is the dominant noise source in our TPL demonstration.* While the roughness of a clean substrate without printed features is  $\sigma = 1.25nm$  (Fig. 13A), the printed flat surface shows roughness of  $\sigma = 15.96nm$ , resulting from the non-periodic line-shaped features post-fabrication. We further plot a height profile of these features along the black dashed line on the flat surface in Fig. 13D, where the randomness in the

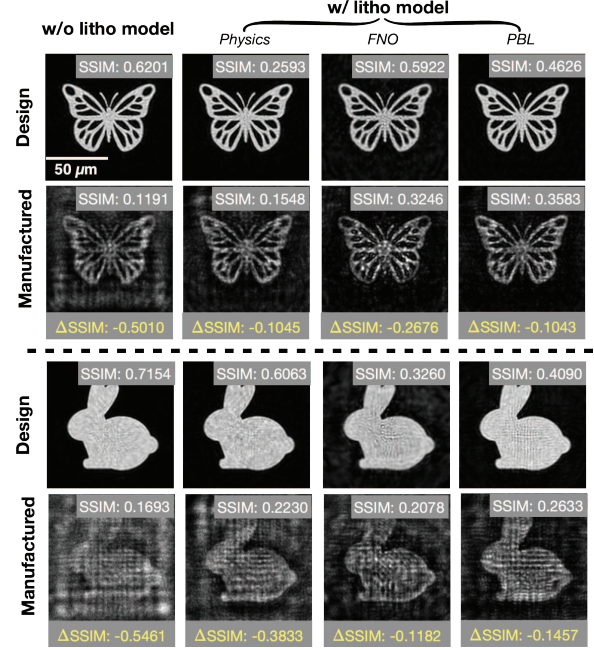


Fig. 11. **Quantitative comparison of holographic images generated by HOE in the design and real experiment.**  $\Delta$ SSIM between the holographic images of the designed and that of manufactured HOEs shows that a huge design-to-manufacturing gap exists for the naive design w/o considering the lithography process. Though not exhibiting good SSIM in the design, the printed HOEs w/ the PBL model result in the best SSIM.

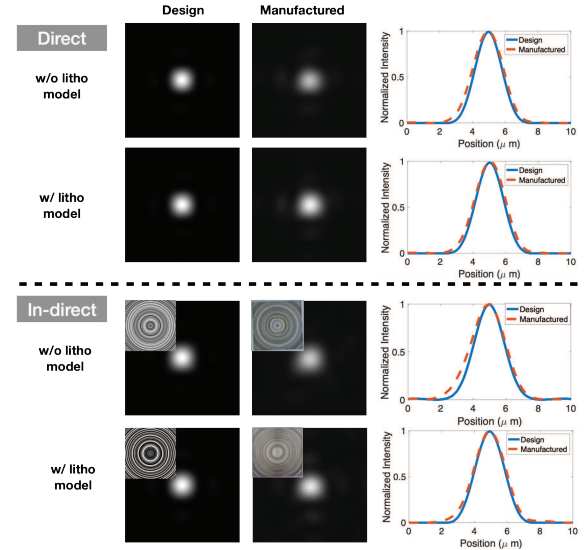


Fig. 12. **Comparison of PSFs generated by MDLs in the design and real experiment.** In both the direct and indirect/computational imaging setting, the naive design w/o lithography model has a larger deviation between the shape from the designed and experimental PSF. In contrast, the deviation is small when we apply neural lithography.



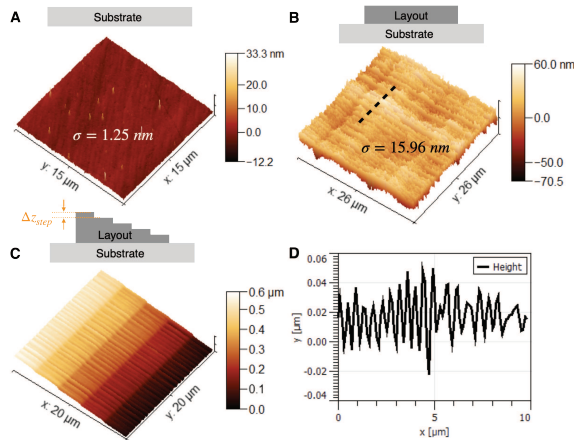


Fig. 13. **Aleatoric uncertainty limits the upper bound of our pipeline's performance.** We measure a clean substrate (A), a flat print (B), and a 5-step print (C) sitting on top of the substrates to visualize and quantify the data noise. The line profile along the black dashed line in B is further visualized in D. The 5-step print with step interval  $\Delta z_{\text{step}} = 0.1\mu\text{m}$  in C shows that the data uniformity is high at a larger scale, while the measured flat surface in B indicates there is a certain degree of uncontrolled noise at the nanoscale from fabrication and measurements. The comparison between A (w/o prints) and B (w/ prints) shows the prints contribute to the most noise. The line profile in D shows strong randomness in the fabrication error, which makes it hard to model.

plot evidences these line-shaped features are hard to model. We also observe these features in the fabricated 5-step structure, but the  $0.1\mu\text{m}$  step size can still be well identified, indicating the structure is well recognized in large structures. Given these, our predicting error of  $\mu = 24.35\text{nm}$  using PBL indicates future room to improve our  $\hat{g}_\theta$ , such as with more training data or more intricate model considering these line-shaped features, or even switching to projective photolithography systems. Nevertheless,  $\sigma = 15.96\text{nm}$  reveals an upper performance bound of current  $\hat{g}_\theta$  given the TPL system we use.

## 5 DISCUSSION

### Limitations:

- The data noise during fabrication and measurement fundamentally limits the optimization capability.
- The neural photolithography simulator has no theoretical guarantees, which might produce adverse designs in the ill-posed inverse design procedures.
- The sim2real gap between simulated and real optical systems impairs performance. The post-calibration methods mitigate the sim2real gap but don't correct the bias from incorrect *f*optics modeling during design.

**Future work:** As a first work on differentiable/neural lithography, our work is poised to inspire future investigations:

*Applying to other design and fabrication processes.* Our real2sim pipeline is adaptable to various lithography techniques, each requiring fine-tuning the model architecture. For example, extreme ultraviolet (EUV) lithography necessitates extra modeling for reflective

projection optics [Wagner and Harned 2010], while etching-based or nanoimprint methods require an added step to transform the resist profile into the final structure [Barcelo and Li 2016]. Similarly, e-beam lithography involves a more complex PSF from electron scattering [Koleva et al. 2018]. Moreover, future work can investigate applying our end-to-end co-optimization pipeline to design and fabricate more complex downstream tasks, such as obtaining depth profile from defocus [Ikoma et al. 2021] and implementing optical computing [Goi et al. 2022].

*Further improving the pipeline.* On the hardware side, other characterization tools, such as 3D SEM [Tafti et al. 2015] or EUV diffractive imaging [Gardner et al. 2017], could be further explored for collecting high-throughput and high-accuracy datasets. On the algorithm side, comprehensive 3D modeling instead of 2.5D will cover more complex resist profiles. We can also further incorporate advanced modeling like neural architecture searching [Ba et al. 2019] to improve the precision of photolithography predictions or utilize implicit neural fields [Yang et al. 2021] to augment the design efficiency of neural lithography.

**Conclusion:** To conclude, our study unveils a unique perspective of jointly optimizing diffractive optical elements in computational optics and their fabrication feasibility. By employing a 'real2sim' learned digital twin of the photolithography system, we enhance the outcomes of optical tasks. This methodology paves the way for the precise manufacturing of sophisticated computational optics elements, expediting their introduction to commercial products. We anticipate that the 'real2sim' approach presented in this paper will encourage both industry and academia to complement traditional white-box methods with the more adaptive, data-driven gray-box methodologies for modeling computational optics systems, as exemplified by the lithography system discussed in our work.

## ACKNOWLEDGMENTS

This work is supported by NIH (5-P41-EB015871), Fujikura Limited, and the Hong Kong Innovation and Technology Fund (ITS/178/20FP). This work was carried out in part using MIT.nano's facilities.

## REFERENCES

- Graham Arthur and Brian Martin. 1996. Investigation of photoresist-specific optical proximity effect. *Microelectronic engineering* 30, 1-4 (1996), 133–136.
- Thomas Auzinger, Wolfgang Heidrich, and Bernd Bickel. 2018. Computational design of nanostructural color for additive manufacturing. *ACM Transactions on Graphics (TOG)* 37, 4 (2018), 1–16.
- Yunhao Ba, Guangyuan Zhao, and Achuta Kadambi. 2019. Blending diverse physical priors with neural networks. *arXiv preprint arXiv:1910.00201* (2019).
- Seung-Hwan Baek, Hayato Ikoma, Daniel S Jeon, Yuqi Li, Wolfgang Heidrich, Gordon Wetzstein, and Min H Kim. 2021. Single-shot hyperspectral-depth imaging with learned diffractive optics. In *Proceedings of the IEEE/CVF International Conference on Computer Vision*. 2651–2660.
- Sourangsu Banerji, Monjurul Meem, Apratim Majumder, Fernando Guevara Vasquez, Berardi Sensale-Rodriguez, and Rajesh Menon. 2019. Imaging with flat optics: metalenses or diffractive lenses? *Optica* 6, 6 (2019), 805–810.
- Steven Barcelo and Zhiyong Li. 2016. Nanoimprint lithography for nanodevice fabrication. *Nano Convergence* 3, 1 (2016), 1–9.
- Atilim Gunes Baydin, Barak A Pearlmutter, Alexey Andreyevich Radul, and Jeffrey Mark Siskind. 2018. Automatic differentiation in machine learning: a survey. *Journal of Machine Learning Research* 18 (2018), 1–43.
- Tomasz Blachowicz, Guido Ehrmann, and Andrea Ehrmann. 2021. Optical elements from 3D printed polymers. *e-Polymers* 21, 1 (2021), 549–565.
- Vivek Boominathan, Jesse K Adams, Jacob T Robinson, and Ashok Veeraraghavan. 2020. Phlatcam: Designed phase-mask based thin lensless camera. *IEEE transactions on pattern analysis and machine intelligence* 42, 7 (2020), 1618–1629.

- Thomas Cecil, Danping Peng, Daniel Abrams, Stanley J Osher, and Eli Yablonovitch. 2022. Advances in Inverse Lithography. *ACS Photonics* (2022).
- Praneeth Chakravarthula, Ethan Tseng, Tarun Srivastava, Henry Fuchs, and Felix Heide. 2020. Learned hardware-in-the-loop phase retrieval for holographic near-eye displays. *ACM Transactions on Graphics (TOG)* 39, 6 (2020), 1–18.
- Pierre Chevalier, Patrick Quéméré, Sébastien Bérard-Bergery, Jean-Baptiste Henry, Charlotte Beylier, and Jérôme Vaillant. 2021. Rigorous Model-Based Mask Data Preparation Algorithm Applied to Grayscale Lithography for the Patterning at the Micrometer Scale. *Journal of Microelectromechanical Systems* 30, 3 (2021), 442–455.
- Suyeon Choi, Manu Gopakumar, Yifan Peng, Jonghyun Kim, Matthew O’Toole, and Gordon Wetzstein. 2022. Time-multiplexed neural holography: a flexible framework for holographic near-eye displays with fast heavily-quantized spatial light modulators. In *ACM SIGGRAPH 2022 Conference Proceedings*. 1–9.
- Nicolas B Cobb, Avideh Zakhor, and Eugene A Miloslavsky. 1996. Mathematical and CAD framework for proximity correction. In *Optical Microlithography IX*, Vol. 2726. SPIE, 208–222.
- Benoît Colson, Patrice Marcotte, and Gilles Savard. 2007. An overview of bilevel optimization. *Annals of operations research* 153 (2007), 235–256.
- Chen-Yuan Dong, Karsten Koenig, and Peter So. 2003. Characterizing point spread functions of two-photon fluorescence microscopy in turbid medium. *Journal of biomedical optics* 8, 3 (2003), 450–459.
- Stephan Dottermusch, Dmitry Busko, Malte Langenhorst, Ulrich W Paetzold, and Bryce S Richards. 2019. Exposure-dependent refractive index of Nanoscribe IP-Dip photoresist layers. *Optics letters* 44, 1 (2019), 29–32.
- Sean D’Silva, Thomas Mülders, Hans-Jürgen Stock, and Andreas Erdmann. 2021. Modeling the impact of shrinkage effects on photoresist development. *Journal of Micro/Nanopatterning, Materials, and Metrology* 20, 1 (2021), 014602–014602.
- Dennis F Gardner, Michael Tanksalvala, Elisabeth R Shanblatt, Xiaoshi Zhang, Benjamin R Galloway, Christina L Porter, Robert Karl Jr, Charles Bevis, Daniel E Adams, Henry C Kapteyn, et al. 2017. Subwavelength coherent imaging of periodic samples using a 13.5 nm tabletop high-harmonic light source. *Nature Photonics* 11, 4 (2017), 259–263.
- Franz J Giessibl. 2003. Advances in atomic force microscopy. *Reviews of modern physics* 75, 3 (2003), 949.
- Elena Goi, Steffen Schoenhardt, and Min Gu. 2022. Direct retrieval of Zernike-based pupil functions using integrated diffractive deep neural networks. *Nature Communications* 13, 1 (2022), 7531.
- Joseph W Goodman. 2005. *Introduction to Fourier optics*. Roberts and Company publishers.
- Dusan Gostimirovic, Dan-Xia Xu, Odile Liboiron-Ladouceur, and Yuri Grinberg. 2022. Deep Learning-Based Prediction of Fabrication-Process-Induced Structural Variations in Nanophotonic Devices. *ACS Photonics* 9, 8 (2022), 2623–2633.
- Vincent Hahn, Pascal Kiefer, Tobias Frenzel, Jingyuan Qu, Eva Blasco, Christopher Barner-Kowollik, and Martin Wegener. 2020. Rapid assembly of small materials building blocks (voxels) into large functional 3D metamaterials. *Advanced Functional Materials* 30, 26 (2020), 1907795.
- V Harinarayana and YC Shin. 2021. Two-photon lithography for three-dimensional fabrication in micro/nanoscale regime: A comprehensive review. *Optics & Laser Technology* 142 (2021), 107180.
- Zhihan Hong, Piaoran Ye, Douglas A Loy, and Rongguang Liang. 2021. Three-dimensional printing of glass micro-optics. *Optica* 8, 6 (2021), 904–910.
- Eyke Hüllermeier and Willem Waegeman. 2021. Aleatoric and epistemic uncertainty in machine learning: An introduction to concepts and methods. *Machine Learning* 110 (2021), 457–506.
- ICRA. 2023. Real2Sim in ICRA 2023. <https://real2sim.com/> Accessed: May 14, 2023.
- Hayato Ikoma, Cindy M Nguyen, Christopher A Metzler, Yifan Peng, and Gordon Wetzstein. 2021. Depth from defocus with learned optics for imaging and occlusion-aware depth estimation. In *2021 IEEE International Conference on Computational Photography (ICCP)*. IEEE, 1–12.
- Intel. 2023. Intel® RealSense™ Depth Camera. <https://www.intelrealsense.com/depth-camera-d415/> Accessed: May 14, 2023.
- Changwon Jang, Kiseung Bang, Minseok Chae, Byoungso Lee, and Douglas Lanman. 2022. Waveguide Holography: Towards True 3D Holographic Glasses. *arXiv preprint arXiv:2211.02784* (2022).
- Changwon Jang, Olivier Mercier, Kiseung Bang, Gang Li, Yang Zhao, and Douglas Lanman. 2020. Design and fabrication of freeform holographic optical elements. *ACM Transactions on Graphics (TOG)* 39, 6 (2020), 1–15.
- Eric Jang, Shixiang Gu, and Ben Poole. 2016. Categorical reparameterization with gumbel-softmax. *arXiv preprint arXiv:1611.01144* (2016).
- Bentian Jiang, Lixin Liu, Yuzhe Ma, Hang Zhang, Bei Yu, and Evangeline FY Young. 2020. Neural-ILT: Migrating ILT to neural networks for mask printability and complexity co-optimization. In *Proceedings of the 39th International Conference on Computer-Aided Design*. 1–9.
- Diederik P Kingma and Jimmy Ba. 2014. Adam: A method for stochastic optimization. *arXiv preprint arXiv:1412.6980* (2014).
- E Koleva, K Vutova, B Asparuhova, I Kostic, K Cvetkov, and V Gerasimov. 2018. Modeling approaches for electron beam lithography. In *Journal of Physics: Conference Series*, Vol. 1089. IOP Publishing, 012016.
- Grace Kuo, Laura Waller, Ren Ng, and Andrew Maimone. 2020. High resolution étendue expansion for holographic displays. *ACM Transactions on Graphics (TOG)* 39, 4 (2020), 66–1.
- Nicolas Lang, Sven Enns, Julian Hering, and Georg von Freymann. 2022. Towards efficient structure prediction and pre-compensation in multi-photon lithography. *Optics Express* 30, 16 (2022), 28805–28816.
- Kyung Chul Lee, Junghyun Bae, Nakkyu Baek, Jaewoo Jung, Wook Park, and Seung Ah Lee. 2023. Design and single-shot fabrication of lensless cameras with arbitrary point spread functions. *Optica* 10, 1 (2023), 72–80.
- Anat Levin, Daniel Glasner, Ying Xiong, Frédo Durand, William Freeman, Wojciech Matusik, and Todd Zickler. 2013. Fabricating BRDFs at high spatial resolution using wave optics. *ACM Transactions on Graphics (TOG)* 32, 4 (2013), 1–14.
- Y Li, S Park, M McLamb, M Lata, S Schöche, D Childers, ID Aggarwal, MK Poutou, G Boreman, and Tino Hofmann. 2019. UV to NIR optical properties of IP-Dip, IP-L, and IP-S after two-photon polymerization determined by spectroscopic ellipsometry. *Optical Materials Express* 9, 11 (2019), 4318–4328.
- Zongyi Li, Nikola Kovachki, Kamyar Azizzadenesheli, Burigede Liu, Kaushik Bhat-tacharya, Andrew Stuart, and Anima Anandkumar. 2020. Fourier neural operator for parametric partial differential equations. *arXiv preprint arXiv:2010.08895* (2020).
- Wei-Ping Liao, Hsueh-Li Liu, Yu-Fan Lin, Sheng-Siang Su, Yu-Teng Chen, Guan-Bo Lin, Tsung-Chieh Tseng, Tong-Ke Lin, Chun-Chi Chen, Wen-Hsien Huang, et al. 2022. I-line photolithographic metalenses enabled by distributed optical proximity correction with a deep-learning model. *Optics Express* 30, 12 (2022), 21184–21194.
- Daniel Christoph Meisel, Marcus Diem, Markus Deubel, Fabián Pérez-Willard, Stefan Linden, Dagmar Gerthsen, Kurt Busch, and Martin Wegener. 2006. Shrinkage precompensation of holographic three-dimensional photonic-crystal templates. *advanced materials* 18, 22 (2006), 2964–2968.
- Christopher A Metzler, Hayato Ikoma, Yifan Peng, and Gordon Wetzstein. 2020. Deep optics for single-shot high-dynamic-range imaging. In *Proceedings of the IEEE/CVF Conference on Computer Vision and Pattern Recognition*. 1375–1385.
- Reut Orange-Kedem, Elias Nehme, Lucien E Weiss, Boris Ferdman, Onit Alalouf, Nadav Opatovski, and Yoav Shechtman. 2021. 3D printable diffractive optical elements by liquid immersion. *Nature communications* 12, 1 (2021), 3067.
- Yifan Peng, Suyeon Choi, Nitish Padmanaban, and Gordon Wetzstein. 2020. Neural holography with camera-in-the-loop training. *ACM Transactions on Graphics (TOG)* 39, 6 (2020), 1–14.
- Amyr Poonawala and Peyman Milanfar. 2007. Mask design for optical microlithography—an inverse imaging problem. *IEEE Transactions on Image Processing* 16, 3 (2007), 774–788.
- Edgar Riba, Dmytro Mishkin, Daniel Ponsa, Ethan Rublee, and Gary Bradski. 2020. Kornia: an open source differentiable computer vision library for pytorch. In *Proceedings of the IEEE/CVF Winter Conference on Applications of Computer Vision*. 3674–3683.
- Charles Roques-Carnes, Zin Lin, Rasmus E Christiansen, Yannick Salamin, Steven E Kooi, John D Joannopoulos, Steven G Johnson, and Marin Soljacic. 2022. Toward 3D-printed inverse-designed metaoptics. *ACS Photonics* 9, 1 (2022), 43–51.
- Sourabh K Saha, Chuck Divin, Jefferson A Cuadra, and Robert M Panas. 2017. Effect of proximity of features on the damage threshold during submicron additive manufacturing via two-photon polymerization. *Journal of Micro and Nano-Manufacturing* 5, 3 (2017).
- Vincent Sitzmann, Steven Diamond, Yifan Peng, Xiong Dun, Stephen Boyd, Wolfgang Heidrich, Felix Heide, and Gordon Wetzstein. 2018. End-to-end optimization of optics and image processing for achromatic extended depth of field and super-resolution imaging. *ACM Transactions on Graphics (TOG)* 37, 4 (2018), 1–13.
- Qilin Sun, Ethan Tseng, Qiang Fu, Wolfgang Heidrich, and Felix Heide. 2020a. Learning rank-1 diffractive optics for single-shot high dynamic range imaging. In *Proceedings of the IEEE/CVF conference on computer vision and pattern recognition*. 1386–1396.
- Qilin Sun, Jian Zhang, Xiong Dun, Bernard Ghanem, Yifan Peng, and Wolfgang Heidrich. 2020b. End-to-end learned, optically coded super-resolution SPAD camera. *ACM Transactions on Graphics (TOG)* 39, 2 (2020), 1–14.
- Synopsys. 2023. S-Litho: Predictive Modeling of Lithographic Processes. <https://www.synopsys.com/silicon/mask-synthesis/sentaurus-lithography.html> Accessed: Aug 27, 2023.
- Ahmad P Tafti, Andrew B Kirkpatrick, Zahrasadat Alavi, Heather A Owen, and Zeyun Yu. 2015. Recent advances in 3D SEM surface reconstruction. *Micron* 78 (2015), 54–66.
- Shiyu Tan, Yicheng Wu, Shou-I Yu, and Ashok Veeraraghavan. 2021. Codedstereo: Learned phase masks for large depth-of-field stereo. In *Proceedings of the IEEE/CVF Conference on Computer Vision and Pattern Recognition*. 7170–7179.
- Ethan Tseng, Shane Colburn, James Whitehead, Luo Cheng Huang, Seung-Hwan Baek, Arka Majumdar, and Felix Heide. 2021. Neural nano-optics for high-quality thin lens imaging. *Nature communications* 12, 1 (2021), 6493.

- Ethan Tseng, Felix Yu, Yuting Yang, Fahim Mannan, Karl ST Arnaud, Derek Nowrouzezahrai, Jean-François Lalonde, and Felix Heide. 2019. Hyperparameter optimization in black-box image processing using differentiable proxies. *ACM Trans. Graph.* 38, 4 (2019), 27–1.
- Ethan Tseng, Yuxuan Zhang, Lars Jebe, Xuaner Zhang, Zhihao Xia, Yifei Fan, Felix Heide, and Jiawen Chen. 2022. Neural Photo-Finishing. *ACM Transactions on Graphics (TOG)* 41, 6 (2022), 1–15.
- Christian Wagner and Noreen Harned. 2010. Lithography gets extreme. *Nature Photonics* 4, 1 (2010), 24–26.
- Hao Wang, Hongtao Wang, Wang Zhang, and Joel KW Yang. 2020. Toward near-perfect diffractive optical elements via nanoscale 3D printing. *ACS nano* 14, 8 (2020), 10452–10461.
- Guandao Yang, Serge Belongie, Bharath Hariharan, and Vladlen Koltun. 2021. Geometry processing with neural fields. *Advances in Neural Information Processing Systems* 34 (2021), 22483–22497.
- Haoyu Yang, Shuhe Li, Yuzhe Ma, Bei Yu, and Evangeline FY Young. 2018. GAN-OPC: Mask optimization with lithography-guided generative adversarial nets. In *Proceedings of the 55th Annual Design Automation Conference*. 1–6.
- Haoyu Yang, Zongyi Li, Kumara Sastry, Saumyadip Mukhopadhyay, Anima Anandkumar, Brucec Khailany, Vivek Singh, and Haoxing Ren. 2022a. Large Scale Mask Optimization Via Convolutional Fourier Neural Operator and Litho-Guided Self Training. *arXiv preprint arXiv:2207.04056* (2022).
- Haoyu Yang, Zongyi Li, Kumara Sastry, Saumyadip Mukhopadhyay, Mark Kilgard, Anima Anandkumar, Brucec Khailany, Vivek Singh, and Haoxing Ren. 2022b. Generic lithography modeling with dual-band optics-inspired neural networks. In *Proceedings of the 59th ACM/IEEE Design Automation Conference*. 973–978.
- Wei Ye, Mohamed Baker Alawieh, Yibo Lin, and David Z Pan. 2019. LithoGAN: End-to-end lithography modeling with generative adversarial networks. In *Proceedings of the 56th Annual Design Automation Conference* 2019. 1–6.
- Shangting You, Jiaao Guan, Jeffrey Alido, Henry H Hwang, Ronald Yu, Leilani Kwe, Hao Su, and Shaochen Chen. 2020. Mitigating scattering effects in light-based three-dimensional printing using machine learning. *Journal of Manufacturing Science and Engineering* 142, 8 (2020), 081002.
- Guangyuan Zhao, Cheng Zheng, Cuifang Kuang, Renjie Zhou, Mohammad M Kabir, Kimani C Toussaint Jr, Wensheng Wang, Liang Xu, Haifeng Li, Peng Xiu, et al. 2018. Nonlinear focal modulation microscopy. *Physical review letters* 120, 19 (2018), 193901.
- Mingdong Zhou, Boyan S Lazarov, and Ole Sigmund. 2014. Topology optimization for optical projection lithography with manufacturing uncertainties. *Applied optics* 53, 12 (2014), 2720–2729.
- Xiaopei Zhu, Zhanhao Hu, Siyuan Huang, Jianmin Li, and Xiaolin Hu. 2022. Infrared invisible clothing: Hiding from infrared detectors at multiple angles in real world. In *Proceedings of the IEEE/CVF Conference on Computer Vision and Pattern Recognition*. 13317–13326.

## A DIFFERENTIATING THROUGH MULTI-LEVEL DIFFRACTIVE OPTICAL ELEMENTS WITH GUMBEL-SOFTMAX TRICK

The leader optimization in the main text requires the pipeline to be fully differentiable. However, the quantization levels of the mask layout are limited in many photolithography fabrication processes, including the two-photon lithography (TPL) system we use in this work. The Nanoscribe TPL system has a minimum axial slicing distance of  $0.1 \mu\text{m}$ . That is to say, it only supports discrete height inputs instead of a continuous height profile between  $0$  and  $2\pi$ , and we calculate that it has 12 discrete levels, leading to  $M \in \mathbb{Z}_{\leq 12}^{n_1 \times n_2}$ , to be random discrete values from  $\mathbb{Z}_{\leq 12} = \{0, 1, \dots, 12\}^2$ . Thus, we apply the Gumbel-Softmax trick [Jang et al. 2016] on the categorical height variables to allow for sampling from the categorical distribution during the forward pass through our lithography simulator. It is worth mentioning that this trick has recently been used in other computational optics tasks [Choi et al. 2022; Zhu et al. 2022].

For each pixel  $r_{pq}$  in the layout  $M$ , we model it follows categorical distribution with class probabilities  $\pi_0, \pi_1, \dots, \pi_{12}$ , corresponding to the  $i = 0, 1, \dots, 12$  categories, i.e., quantized phase levels.

<sup>2</sup>Here we abuse the use of notations. Normally  $\mathbb{Z}$  contains  $\{\dots, -2, -1, 0, 1, 2, \dots\}$  and here we refer it as  $\{0, 1, 2, \dots\}$ .

We introduce Gumbel noise to add randomness to the sampling procedure.

$$g_i = -\log(-\log(u_i)), \quad u_i \sim \text{Uniform}(0, 1), \quad (11)$$

where  $g_i$  is the Gumbel noise. We then calculate the vector  $y_i$  using softmax as a differentiable approximation to the argmax-based sampling:

$$y_i = \text{Softmax}[(g_i + \log \pi_i)/\tau], \quad (12)$$

where we choose temperature  $\tau = 0.5$  in our experiment. See more explanations of Gumble-Softmax in [Jang et al. 2016].

## B FABRICATION AND CHARACTERIZATION

### B.1 Mask and optical elements fabrication

We fabricate the masks in dataset  $\mathcal{D}$  and computational optical elements in downstream tasks using a commercial two-photon lithography system – Photonic Professional GT2 (Nanoscribe GmbH). We use a  $63\times/1.4\text{NA}$  objective, IP-Dip photoresist, and a  $25\text{mm}\times 25\text{mm}\times 0.7\text{mm}$  fused silica glass substrate.

We follow the printing parameter set according to [Wang et al. 2020], reproducing very well in our task. The writing parameters for the photolithography process are fixed for all prints: the ratio of laser power 50%, scan speed  $40000 \mu\text{m/s}$ , and hatching and slicing distance of  $0.1 \mu\text{m}$ .

The laser power ratio is critical for the lithography performance. We grid-search the laser power in case it leads to poor manufacturing. As seen from Fig. 14, a laser power 50% is the most suitable for printing the structure and would neither over- nor under-expose the photoresist.

A  $1\text{-}\mu\text{m}$ -thick base layer is printed with the same parameters before printing the structures to compensate for errors in identifying the position of the substrate and resist interface. After photopolymerization, the structures are developed in resist developer polyethylene glycol methyl ether acetate (PGMEA) for 20 min, followed by immersion in isopropyl alcohol for 5 min. Then, we use a nitrogen gun to dry the structures before deployment.

### B.2 Prints characterization

We measure the height profiles of the fabricated structures using Jupiter XR atomic force microscope (AFM) (Asylum Research, Oxford Instruments). We choose to use the AFM based on the performance comparison of the three mainstream methods: the Profilometer [Hong et al. 2021], SEM [Liao et al. 2022], and AFM [Chevalier et al. 2021], which all have been used for characterizing the nano-optical prints before. AFM provides quantitative information on structure height with a high lateral resolution, while SEM doesn't have quantitative height information, and Profilometer doesn't have enough lateral resolution.

We acquire the AFM images with a  $0.1\mu\text{m}$  scanning pixel size. We then process the images in Gwyddion<sup>3</sup> software to remove the background with  $2^{\text{nd}}$  order polynomial fit and shift the minimum height value to 0.

<sup>3</sup><http://gwyddion.net/>



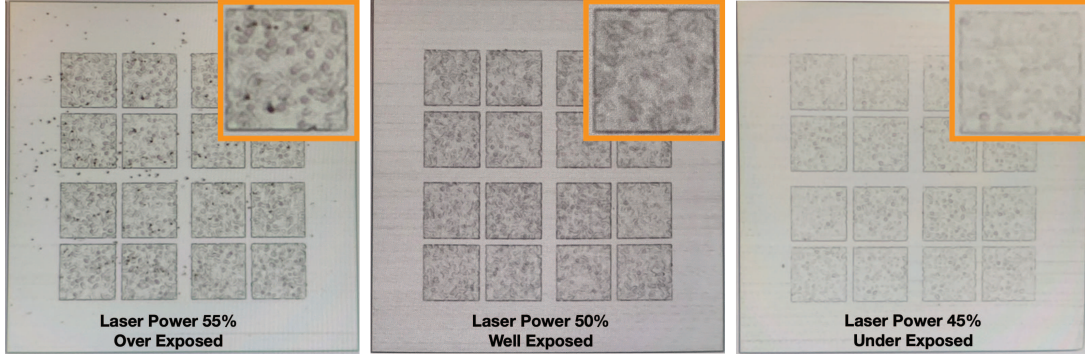


Fig. 14. 50% laser power is suitable for the lithography system we use.

	Profilometer	SEM	AFM
Lateral Resolution	Low	High	High
Speed	Fast	Medium	Slow
Dimension	2.5D	2D	2.5D

Table 2. **Comparison of characterization methods used in the nano-optics.** Though slow in acquisition speed, AFM offers the required 2.5D and high-lateral resolution imaging capability and thus becomes the best option for this work.

## C GENERATE RANDOMIZED PRINTING LAYOUT

To efficiently explore the design space of layout  $M$  to train a  $\hat{g}_\theta$  for the inverse design, we design the height layout  $\mathbf{M}_i \in \mathbb{Z}_{\leq 12}^{n_1 \times n_2}$  ( $i \in \{1, 2, 3, \dots, 96\}$ ) to be random discrete values from  $\mathbb{Z}_{\leq 12} = \{0, 1, \dots, 12\}$ . The mathematical operation to synthesize  $\mathbf{M}_i$  is in Eq. 13, modified from [Gostimirovic et al. 2022]. We sample a matrix  $\mathbf{R}_i \in \mathbb{R}^{n_1 \times n_2}$  with each entry  $r_{pq} \sim U(0, 1)$ . We then apply a low-pass filter (LPF) on the Fourier transform  $\mathcal{F}$  of this random matrix  $\mathbf{R}_i$  to remove the high-frequency structural components; an inverse Fourier transform  $\mathcal{F}^{-1}$  is applied on the normalized real part of it. Finally, we apply a quantization step  $Q$ , which quantizes the layout pixel values to  $\mathbb{Z}_{\leq 12}$ .

$$\mathbf{M}_i = Q(\text{norm} \{ \Re \{ \mathcal{F}^{-1} \{ \mathcal{F} \{ \mathbf{R}_i \} \cdot \text{LPF} \} \} \}), \quad (13a)$$

$$Q(\cdot) = \Delta \times \lfloor \frac{\cdot}{\Delta} + \frac{1}{2} \rfloor, \quad (13b)$$

where  $\Delta = \frac{1}{12}$  is the step size for the quantization, *norm* denotes normalizing the input to  $[0, 1]$ . The final layouts contain structures of lateral sizes ranging from  $0.1 \mu\text{m}$  to several microns.

## D MODEL ARCHITECTURE AND TRAINING SETTINGS

### D.1 Training details

When training the forward model  $\hat{g}_\theta$  in the main text, we split the dataset  $\mathcal{D}$  to train set size 72 and validation set size 24. We compare the three models: the PBL, the Fourier Neural Operator (FNO), and the parameterized physics model. These three models are trained using the Adam optimizer [Kingma and Ba 2014] and a batchsize of 4 for 4000 epochs. Specifically, the learning rate for

training the PBL model is 0.0005. Note that the neural lithography simulator should be retrained for every new fabrication system or a new photoresist/protocol.

### D.2 Model architecture

*D.2.1 More details on the PBL model.* Table 3 summarizes the learnable parameters  $\theta$  in lithography simulator  $\hat{g}_\theta$ . There are single-value parameters in the corresponding Gaussian kernels and learnable weights and biases of the convolution layers inside each neural operator.

We do not include  $\sigma_{\text{optical}}$  into  $\theta$  as it is deterministic concerning the optical setup.  $\sigma_{\text{optical}}$  is fixed as  $200 \text{ nm}$ , calculated according to the beam focused by the illumination objective lens [Dong et al. 2003].  $\sigma_{\text{diffusion}}$  is learnable. To limit  $\sigma_{\text{diffusion}}$ 's range during the training, we further model  $\sigma_{\text{diffusion}}$  as:

$$\sigma_{\text{diffusion}} = \frac{\eta}{1 + e^{-\tau}}, \quad (14)$$

where  $\eta$  is a hyper-parameter to limit the value range, and  $\tau$  is the underlying learnable parameter. Specifically, in this work, we determine  $\sigma_{\text{diffusion}}$ 's value range to be  $[0, 2.5 \mu\text{m}]$  according to [Lang et al. 2022] and thus set the hyper-parameter  $\eta = 2.5 \mu\text{m}$ .

Function	Parameter
$g_{\text{thresh}}$	Weights and biases
$h_{\text{diffusion}}$	$\tau$
$g_{\text{shrink}}$	Weights and biases
$g_{\text{mismatch}}$	Weights and biases

Table 3. **Learnable parameters included in  $\theta$  in PBL.**

We apply the pointwise and areawise neural networks inside the physics-based neural network to model the corresponding operations inspired by the work from [Tseng et al. 2022].

*Pointwise neural operator* is used in  $g_{\text{thresh}}$  and  $g_{\text{shrink}}$ . It affects the input at a pixel-wise level without affecting neighboring pixels. As summarized in Table 4 below, it consists of three convolution layers using a  $1 \times 1$  kernel, each followed by a Leaky Relu activation function (with the hyper-parameter negative slope  $\alpha = 0.02$ ) except for the last layer.

*Areawise neural operator* is used in  $g_{\text{mismatch}}$ . It is a nonlinear filter that depends on patches or segments of the input (e.g., regions

Layer Name	Output Channels	Kernel Size	Activation
Conv1	128	1 × 1	LeakyReLU
Conv2	64	1 × 1	LeakyReLU
Conv3	1	1 × 1	-

Table 4. Neural pointwise operator architecture.

of an image) rather than individual pixels. Thus, we use convolution layers with kernel size as a  $3 \times 3$  and padding size as 1. Table 5 below shows five convolution layers, each followed by a Leaky Relu activation function ( $\alpha = 0.02$ ) except for the last layer.

Layer Name	Output Channels	Kernel Size	Activation
Conv1	64	$3 \times 3$	LeakyReLU
Conv2	64	$3 \times 3$	LeakyReLU
Conv3	32	$3 \times 3$	LeakyReLU
Conv4	32	$3 \times 3$	LeakyReLU
Conv5	1	$3 \times 3$	-

Table 5. Neural areawise operator architecture.

**D.2.2 Fourier Neural Operator (FNO).** Our implementation of the FNO model is adapted from FNO2d in [Li et al. 2020]. Key hyper-parameters are:  $modes_1 = 12$ ;  $modes_2 = 12$ ;  $width = 24$ . We use a learning rate of 0.0001 for training the FNO model.

**D.2.3 Parameterized physics model (Physics).** The parameterized physics model is modified from our PBL model but substitutes the neural network modules with parameterized functions. Modifications include:

- Substituting the pointwise neural network  $g_{\text{thresh}}$  with a normalized projection [Zhou et al. 2014]:

$$\hat{H}_{\text{init}} = \frac{\tanh(\alpha\eta) + \tanh(\alpha(I_{\text{optical}} - \eta))}{\tanh(\alpha\eta) + \tanh(\alpha(1 - \eta))}, \quad (15)$$

where  $\alpha$  and  $\eta$  are learnable single-value parameters. The function does not differ too much from sigmoid (normally used to represent the threshold behavior of photoresist) when  $\alpha$  is large. We use it because, for a small  $\alpha$ , this function is better as it interpolates the whole interval  $[0,1]$ , but the sigmoid function does not.

- Substituting the pointwise neural network  $g_{\text{shrink}}$  with a linear mapping operation used in [Lang et al. 2022]:

$$S = \frac{\kappa_{\text{max}} - \kappa_{\text{min}}}{\max(I_{\text{diffusion}}) - \min(I_{\text{diffusion}})}, \quad (16)$$

where  $\kappa_{\text{min}}$  is the learnable single-value parameter and  $\kappa_{\text{max}}$  is fixed to be 1.

- Substituting the areawise neural network  $g_{\text{mismatch}}$  with a learnable single-value height bias  $b$ .

To summarize, in the parameterized physics model, they are 5 learnable single-value parameters:  $\alpha$ ,  $\eta$ ,  $\kappa_{\text{min}}$ ,  $b$  and  $\sigma_{\text{diffusion}}$ , which is used to parameterize the kernel for the diffusion of reactants. The learning rate for training the parameterized physics model is 0.01.

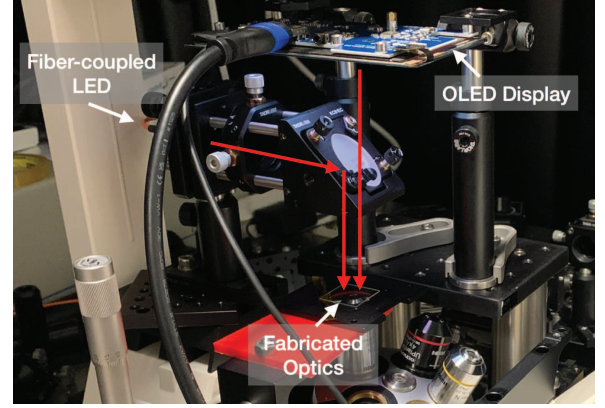


Fig. 15. Experimental setup for assessing the performance of HOE and MDL. The fiber-coupled LED calibrates the point spread function (PSF) in the MDL task or generates the holographic image in the HOE task. The OLED display here acts as the object for the MDL imaging task.

## E ADDITIONAL EXPERIMENTAL DETAILS

The experimental setup in Fig. 15, incorporates two illumination sources. For holographic imaging and the acquisition of the PSF, we utilize a fiber-coupled LED collimated to pass through a pin-hole and then reflected by a mirror onto the fabricated optics. In MDL imaging, the fiber-coupled LED beam path is removed, and an OLED display serves as the object with dimensions of  $36 \text{ mm}$ . The exposure times for capturing holographic and MDL images are 3 s and 5 s, respectively. These extended durations are attributable to low illumination power and camera quantum efficiency. We also note the presence of dead pixels on the camera (CMOS, FLIR GS3-U3-32S4M-C), manifesting as random bright spots on the captured images, further compromising image quality.